INTERNATIONAL JOURNAL FOR NUMERICAL METHODS IN ENGINEERING, VOL. 37, 229–256 (1994)

ELEMENT-FREE GALERKIN METHODS

T. BELYTSCHKO, Y. Y. LU AND L. GU

Department of Civil Engineering, Robert R. McCormick School of Engineering and Applied Science, The Technological Institute, Northwestern University, Evanston IL 60208-3109, U.S.A.

SUMMARY

An element-free Galerkin method which is applicable to arbitrary shapes but requires only nodal data is applied to elasticity and heat conduction problems. In this method, moving least-squares interpolants are used to construct the trial and test functions for the variational principle (weak form); the dependent variable and its gradient are continuous in the entire domain. In contrast to an earlier formulation by Nayroles and coworkers, certain key differences are introduced in the implementation to increase its accuracy. The numerical examples in this paper show that with these modifications, the method does not exhibit any volumetric locking, the rate of convergence can exceed that of finite elements significantly and a high resolution of localized steep gradients can be achieved. The moving least-squares interpolants and the choices of the weight function are also discussed in this paper.

INTRODUCTION

In recent years, it has become clear that in linear analysis, mesh generation is a far more time-consuming and expensive task than the assembly and solution of the finite element equations. Therefore, it has become expedient to explore methods which may be somewhat more expensive from the viewpoint of computer time but involve less time in the preparation of data. In this respect, it might be mentioned that even with powerful mesh generators, three-dimensional meshing is still an extremely burdensome task and that the conversion of solid models to finite element data is time-consuming and often introduces numerous ambiguities.

Nayroles *et al.*[1] have recently introduced a very interesting and promising method which they call the diffuse element method. In this method, only a mesh of nodes and a boundary description is needed to develop the Galerkin equations. The interpolants are polynomials which are fit to the nodal values by a least-squares approximation. The finite element mesh is totally unnecessary in this method.

Although not noted by Nayroles *et al.*[1] (1992), the interpolants used in their method were introduced and studied by Lancaster and Salkauskas,[2] McLain,[3] Gordon and Wixom,[4] Barnhill[5] and called moving least-squares (MLS) interpolants in curve and surface fitting. Moving least-squares methods interpolants do not pass through the data because the interpolation functions are not equal to unity at the nodes unless the weighting functions are singular. This is of disadvantage in Galerkin methods for it complicates the imposition of essential boundary conditions and the application of point loads. However, these disadvantages are so heavily outweighed by the potential savings which are brought about by the absence of elements and the consequent avoidance of element meshing that the method looks very promising indeed. Because the circumvention of the need for element data is the key advantage of the method, we have here called Galerkin method with moving least-squares interpolant the element-free Galerkin method, EFG method.

0029–5981/94/020229–28$19.00

Received 4 April 1993
Revised 12 May 1993

The essential idea of MLS interpolants is that it is only necessary to construct an array of nodes in the domain under consideration. Thus, the method is completely element-free but can be imbued with the generality of a finite element method, and by an appropriate construction of the method, it can be very easily coupled with CAD data. Even more exciting are its potential in adaptive methods, where in an interactive mode a user could simply drop large number of points into the portion of a component where he would like more accuracy and the method would precede to enhance the solution without constructing a new finite element mesh. This development is particularly promising because the accuracy of the method does not appear to deteriorate if the placement of the nodes is very irregular.

This paper presents an implementation which differs from Nayroles *et al.*[1] and some introductory studies of the method in two-dimensional problems of heat conduction and elasticity. There are three major findings we would like to report about the implementation we have developed:

1. the element-free Galerkin method does not seem to exhibit any volumetric locking even when the basis functions are linear,
2. the rate of convergence for the method in this implementations can exceed that of finite elements significantly,
3. a high resolution of localized steep gradients can be achieved by this method,
4. the method is very effective in linear elastic fracture problems.

These findings hinge to a large extent on some differences between the implementation of Nayroles *et al.*[1] and the implementation we have developed. The major differences are

1. We have used a large number of quadrature points arranged in a cell structure that overlays the domain.
2. We have included certain terms in the derivatives of the interpolants which were omitted by Nayroles *et al.*[1]
3. We have used Lagrange multipliers to enforce essential boundary conditions.

This approach is not as versatile as the Nayroles *et al.*[1] implementation, but we feel it is justified by the increase in accuracy. In contrast to other methods for arbitrary grid spacings, such as Nay and Utku[6] than in smooth particle methods,[7] finite difference formulas are not constructed in this method, and accuracy appears to be higher. Since this class of methods is in its infancy, large number of issues need to be addressed and we will outline some of these issues and give some indications of how these problems can be addressed. Finally, numerical results are given which indicate the rate of convergence and the power of the method.

MOVING LEAST-SQUARES INTERPOLANT

The moving least squares (MLS) interpolant $u^h(\mathbf{x})$ of the function $u(\mathbf{x})$ is defined in the domain Ω by

$$u^h(\mathbf{x}) = \sum_j^m p_j(\mathbf{x})\, a_j(\mathbf{x}) \equiv \mathbf{p}^{\mathrm{T}}(\mathbf{x})\, \mathbf{a}(\mathbf{x}) \tag{1}$$

where $p_1(\mathbf{x}) = 1$ and $p_j(\mathbf{x})$ are monomials in the space co-ordinates $\mathbf{x}^{\mathrm{T}} = [x, y]$ so that the basis is complete. A linear basis in one dimension is provided by

$$\mathbf{p}^{\mathrm{T}}(\mathbf{x}) = [1, x], \quad m = 2 \tag{2a}$$

and a quadratic basis by

$$\mathbf{p}^{\mathrm{T}}(\mathbf{x}) = [1, x, x^2], \quad m = 3 \tag{2b}$$

whereas a linear basis in a two-dimensional domain is provided by

$$\mathbf{p}^{\mathrm{T}}(\mathbf{x}) = [1, x, y], \quad m = 3 \tag{3a}$$

and a quadratic basis by

$$\mathbf{p}^{\mathrm{T}}(\mathbf{x}) = [1, x, y, x^2, xy, y^2], \quad m = 6 \tag{3b}$$

The coefficients $a_j(\mathbf{x})$ in equation (1) are also functions of $\mathbf{x}$; $\mathbf{a}(\mathbf{x})$ is obtained at any point $\mathbf{x}$ by minimizing a weighted, discrete L_2 norm as follows:

$$J = \sum_I^n w(\mathbf{x} - \mathbf{x}_I)[\mathbf{p}^{\mathrm{T}}(\mathbf{x}_I)\mathbf{a}(\mathbf{x}) - u_I]^2 \tag{4}$$

where n is the number of points in the neighbourhood of $\mathbf{x}$ for which the weight function $w(\mathbf{x} - \mathbf{x}_I) \neq 0$, and u_I is the nodal value of u at $\mathbf{x} = \mathbf{x}_I$. This neighbourhood of $\mathbf{x}$ is called the domain of influence of $\mathbf{x}$, or circle of influence in two dimensions.

The stationarity of J in equation (4) with respect to $\mathbf{a}(\mathbf{x})$ leads to the following linear relation between $\mathbf{a}(\mathbf{x})$ and u_I:

$$\mathbf{A}(\mathbf{x})\mathbf{a}(\mathbf{x}) = \mathbf{B}(\mathbf{x})\mathbf{u} \tag{5}$$

or

$$\mathbf{a}(\mathbf{x}) = \mathbf{A}^{-1}(\mathbf{x})\mathbf{B}(\mathbf{x})\mathbf{u} \tag{6}$$

where $\mathbf{A}(\mathbf{x})$ and $\mathbf{B}(\mathbf{x})$ are the matrices defined by

$$\mathbf{A}(\mathbf{x}) = \sum_I^n w_I(\mathbf{x})\mathbf{p}^{\mathrm{T}}(\mathbf{x}_I)\mathbf{p}(\mathbf{x}_I), \quad w_I(\mathbf{x}) \equiv w(\mathbf{x} - \mathbf{x}_I) \tag{7}$$

$$\mathbf{B}(\mathbf{x}) = [w_1(\mathbf{x})\mathbf{p}(\mathbf{x}_1), w_2(\mathbf{x})\mathbf{p}(\mathbf{x}_2), \ldots, w_n(\mathbf{x})\mathbf{p}(\mathbf{x}_n)] \tag{8}$$

$$\mathbf{u}^{\mathrm{T}} = [u_1, u_2, \ldots, u_n] \tag{9}$$

Hence, we have

$$u^h(\mathbf{x}) = \sum_I^n \sum_j^m p_j(\mathbf{x})(\mathbf{A}^{-1}(\mathbf{x})\mathbf{B}(\mathbf{x}))_{jI} u_I \equiv \sum_I^n \phi_I(\mathbf{x}) u_I \tag{10}$$

where the shape function $\phi_I(\mathbf{x})$ is defined by

$$\phi_I(\mathbf{x}) = \sum_j^m p_j(\mathbf{x})(\mathbf{A}^{-1}(\mathbf{x})\mathbf{B}(\mathbf{x}))_{jI} \tag{11}$$

The partial derivatives of $\phi_I(\mathbf{x})$ can be obtained as follows:

$$\phi_{I,i} = \sum_j^m \{p_{j,i}(\mathbf{A}^{-1}\mathbf{B})_{jI} + p_j(\mathbf{A}_{,i}^{-1}\mathbf{B} + \mathbf{A}^{-1}\mathbf{B}_{,i})_{jI}\} \tag{12}$$

where

$$\mathbf{A}_{,i}^{-1} = -\mathbf{A}^{-1}\mathbf{A}_{,i}\mathbf{A}^{-1} \tag{13}$$

and the index following a comma is a spatial derivative. It should be noted that the approximation (10) is no longer a polynomial even if the basis functions $\mathbf{p}(\mathbf{x})$ are polynomials. However, if $u(\mathbf{x})$ is a polynomial, it is reproduced exactly by $u^h(\mathbf{x})$; see Nayroles *et al.*[1] Moreover, if the weight function $w_I(\mathbf{x})$ is continuous together with its first k derivatives, the shape function $\phi_I(\mathbf{x})$ is also continuous together with its first k derivatives.[2] Typically, if $k = \infty$, then $\phi_I(\mathbf{x}) \in C^\infty$. Moreover, for accurate results, the coefficient $\mathbf{a}(\mathbf{x})$ in equation (10) should not be assumed to be constant, i.e.

the term $(\mathbf{A}_{,i}^{-1}\mathbf{B} + \mathbf{A}^{-1}\mathbf{B}_{,i})_{jI}$ cannot be neglected in equation (12). We shall show in the numerical examples that not accounting for the spatial variation of $\mathbf{a}(\mathbf{x})$ detracts significantly from the accuracy of the method.

Remark 1. The standard least-squares interpolant is obtained if the weight function $w_I(\mathbf{x})$ is chosen to be constant over the entire domain. However, all unknowns are then fully coupled. By choosing $w_I(\mathbf{x})$ to have a large domain of influence, the interpolant behaves like a polynomial of higher order than $p(\mathbf{x})$; limiting it to be non-zero over a small subdomain results in a sparse system of equations.

Remark 2. The standard finite element method can also be obtained if the weight function $w_I(\mathbf{x})$ is defined as piecewise-constant over each subdomain or element.

CHOICE OF WEIGHT FUNCTION

The weight functions $w_I(\mathbf{x}) \equiv w(\mathbf{x} - \mathbf{x}_I)$ play an important role in the performance of the method. They should be constructed so that they are positive and that a unique solution $\mathbf{a}(\mathbf{x})$ is guaranteed; they should be relatively large for the $\mathbf{x}_I$ close to $\mathbf{x}$, and relatively small for the more distant $\mathbf{x}_I$; in other words, they should decrease in magnitude as the distance from $\mathbf{x}$ to $\mathbf{x}_I$ increases. Therefore, we will consider weight functions which depend only on the distance between two points as follows:

$$w(\mathbf{x} - \mathbf{x}_I) = w_I(d) \tag{14}$$

where $d = \|\mathbf{x} - \mathbf{x}_I\|$ is the distance between the two points $\mathbf{x}$ and $\mathbf{x}_I$. More specifically we consider the weight functions of the following form:

$$w_I(\mathbf{x}) \equiv w_I(d^{2k}) \tag{15}$$

where $w_I(d^{2k})$ is assumed to be continuous together with its first m derivatives with respect to d.

We now consider conditions which the constant k must satisfy to assure that the first n derivatives of weight function $w_I(d^{2k})$ with respect to x or y in two dimension exist at the data point $\mathbf{x}_I$. To begin, we consider the derivative of weight function $w_I(d^{2k})$ with respect to x:

$$\frac{\partial w_I}{\partial x} = 2k d^{2k-1}\frac{\partial w_I}{\partial d}\frac{\partial d}{\partial x} = 2k(x - x_I)d^{2k-2}\frac{\partial w_I}{\partial d} \quad \text{in 2D} \tag{16}$$

Note that the limit of $(x - x_I)/d$ as $\mathbf{x}$ approaches $\mathbf{x}_I$ does not exist. Therefore, the above derivative exists only if $k > 1/2$. For the second derivative of the weight function $w_I(d^{2k})$ with respect to x, we have

$$\frac{\partial^2 w_I}{\partial^2 x} = 2k(2k-2)(x - x_I)^2 d^{2k-4}\frac{\partial w_I}{\partial d} + 2k d^{2k-2}\frac{\partial w_I}{\partial d} + 4k^2(x - x)^2 d^{4k-4}\frac{\partial^2 w_I}{\partial^2 d} \quad \text{in 2D} \tag{17}$$

Therefore, the above derivative exists if $k \geqslant 1$. By calculating the nth derivative of weight function $w_I(d^{2k})$ with respect to x, we have the following conclusions for two-dimensional problems:

(i) If k is a positive integer, the derivative of the weight function $w_I(d^{2k})$ with respect to x or y exists up to mth order.

(ii) If k is not a positive integer but $k > n/2$ then the derivative of weight function $w_I(d^{2k})$ with respect to x or y exists at least up to nth order.

The choice of weight function is more or less arbitrary as long as the weight function is positive and continuous together with its derivatives up to the desired degree. To examine the effect of

different kinds of weight functions on EFG, we have considered two types of weight functions in this paper:

Exponential weight function:

$$w_I(d_I^{2k}) = \begin{cases} \dfrac{e^{-(d_I/c)^{2k}} - e^{-(d_{mI}/c)^{2k}}}{(1 - e^{-(d_{mI}/c)^{2k}})}, & d_I \leqslant d_{mI}, \\ 0, & d_I > d_{mI} \end{cases} \tag{18}$$

Conical weight function:

$$w_I(d_I^{2k}) = \begin{cases} 1 - (d_I/d_{mI})^{2k}, & d_I \leqslant d_{mI} \\ 0, & d_I > d_{mI} \end{cases} \tag{19}$$

In the above, c is a constant which controls the relative weights and $d_I = \|\mathbf{x} - \mathbf{x}_I\|$; d_{mI} is the size of the support for the weight function $w_I(d_I^{2k})$ and determines the domain of influence of $\mathbf{x}_I$. It should be chosen so that the matrix $\mathbf{A}$ in equation (6) in not singular. In this paper, whenever we refer to stable values of the parameter d_{mI}, it is implied that the inverse of matrix $\mathbf{A}$ in equation (6) exists for these values of d_{mI}.

Note that when c decreases, we obtain higher weights on points $\mathbf{x}_I$ close to $\mathbf{x}$ and lower weights on points far removed from $\mathbf{x}$. In this paper, we define c as follows:

$$c = \alpha c_I \tag{20}$$

where we have used $1 \leqslant \alpha \leqslant 2$ and

$$c_I = \max_{J \in S_J} \|\mathbf{x}_J - \mathbf{x}_I\| \tag{21}$$

where S_J is minimum set of neighbouring points of $\mathbf{x}_I$ which construct a polygon surrounding point $\mathbf{x}_I$. If the nodes are uniformly distributed, then c_I in equation (21) is the maximum distance between nodes. In the case where the nodes are randomly distributed, c_I can be defined as a characteristic length of the integration zone that contains the point $\mathbf{x}_I$. Of course, other choices for c_I are also possible. The performance of the above weight functions with $k = 1$ will be examined in numerical examples.

VARIATIONAL FORM AND LAGRANGE MULTIPLIERS

We consider the following two-dimensional problem on the domain Ω bounded by Γ:

$$\nabla \cdot \boldsymbol{\sigma} + \mathbf{b} = \mathbf{0} \quad \text{in } \Omega \tag{22}$$

where $\boldsymbol{\sigma}$ is the stress tensor, which corresponds to the displacement field $\mathbf{u}$ and $\mathbf{b}$ is a body force vector. The boundary conditions are given as follows:

$$\boldsymbol{\sigma} \cdot \mathbf{n} = \bar{\mathbf{t}} \quad \text{on } \Gamma_t \tag{23}$$

$$\mathbf{u} = \bar{\mathbf{u}} \quad \text{on } \Gamma_u \tag{24}$$

in which the superposed bar denotes prescribed boundary values, and $\mathbf{n}$ is the unit normal to the domain Ω.

The variational (or weak) form of the equilibrium equation is posed as follows. Consider trial functions $\mathbf{u}(\mathbf{x}) \in H^1$ and Lagrange multipliers $\lambda \in H^0$, test functions $\delta\mathbf{v}(\mathbf{x}) \in H^1$ and $\delta\lambda \in H^0$, then

if

$$\int_\Omega \delta(\nabla_s \mathbf{v}^T) : \boldsymbol{\sigma}\, d\Omega - \int_\Omega \delta \mathbf{v}^T \cdot \mathbf{b}\, d\Omega - \int_{\Gamma_t} \delta \mathbf{v}^T \cdot \bar{\mathbf{t}}\, d\Gamma$$
$$- \int_{\Gamma_u} \delta\lambda^T \cdot (\mathbf{u} - \bar{\mathbf{u}})\, d\Gamma - \int_{\Gamma_u} \delta \mathbf{v}^T \cdot \lambda\, d\Gamma = 0 \quad \forall \delta \mathbf{v} \in H^1,\ \delta\lambda \in H^0 \tag{25}$$

then equilibrium equation (22) and the boundary conditions (23) and (24) are satisfied. Here $\nabla_s \mathbf{v}^T$ is the symmetric part of $\nabla \mathbf{v}^T$; H^1 and H^0 denote the Sobolev spaces of degree one and zero, respectively. Note that the trial functions do not satisfy the essential boundary conditions, so that they are imposed by Lagrange multipliers.

In order to obtain the discrete equation from the weak form (25), the approximate solution $\mathbf{u}$ and the test function $\delta \mathbf{v}$ are constructed according to equation (10). The Lagrange multiplier λ is expressed by

$$\lambda(\mathbf{x}) = N_I(s)\, \lambda_I, \quad \mathbf{x} \in \Gamma_u \tag{26}$$

$$\delta\lambda(\mathbf{x}) = N_I(s)\, \delta\lambda_I, \quad \mathbf{x} \in \Gamma_u \tag{27}$$

where $N_I(s)$ is a Lagrange interpolant and s is the arclength along the boundary; the repeated indices designate summations. The final discrete equations can be obtained by substituting the trial functions, test functions and equations (26) and (27) into the weak form (25), which yields

$$\begin{bmatrix} \mathbf{K} & \mathbf{G} \\ \mathbf{G}^T & \mathbf{0} \end{bmatrix} \begin{Bmatrix} \mathbf{u} \\ \lambda \end{Bmatrix} = \begin{Bmatrix} \mathbf{f} \\ \mathbf{q} \end{Bmatrix} \tag{28}$$

and

$$\mathbf{K}_{IJ} = \int_\Omega \mathbf{B}_I^T \mathbf{D} \mathbf{B}_J\, d\Omega \tag{29a}$$

$$\mathbf{G}_{IK} = -\int_{\Gamma_u} \phi_I N_K\, d\Gamma \tag{29b}$$

$$\mathbf{f}_I = \int_{\Gamma_t} \phi_I \bar{\mathbf{t}}\, d\Gamma + \int_\Omega \phi_I \mathbf{b}\, d\Omega \tag{29c}$$

$$\mathbf{q}_K = -\int_{\Gamma_u} N_K \bar{\mathbf{u}}\, d\Gamma \tag{29d}$$

where

$$\mathbf{B}_I = \begin{bmatrix} \phi_{I,x} & 0 \\ 0 & \phi_{I,y} \\ \phi_{I,y} & \phi_{I,x} \end{bmatrix} \tag{30a}$$

$$\mathbf{N}_K = \begin{bmatrix} N_k & 0 \\ 0 & N_K \end{bmatrix} \tag{30b}$$

$$\mathbf{D} = \frac{E}{1-\upsilon^2} \begin{bmatrix} 1 & \upsilon & 0 \\ \upsilon & 1 & 0 \\ 0 & 0 & (1-\upsilon)/2 \end{bmatrix} \text{ for plane stress} \tag{30c}$$

in which a comma designates a partial derivative with respect to the indicated spatial variable; E and υ are Young's modulus and Poisson's ratio, respectively. Note that the coefficient matrix in equation (28) is symmetric but not positive-definite. In heat conduction, the unknown is a scalar and the counterpart can be found in most finite element textbooks such as Zienkiewicz and Taylor.[8]

In order to obtain the integrals in equations (29a)–(29d), a cell structure which is independent of the nodes is used. Such types of data structures, often called buckets, are widely used in contact-impact algorithms and other search algorithms, see Benson and Hallquist[9] or Belytschko and Lin.[10] This procedure is illustrated in Figure 1.

The domains of influence of two typical points is also shown in Figure 1. As can be seen, the domain of influence of a point never extends across any boundaries. Thus, for a quadrature point next to a crack, the domain of influence of $\mathbf{x}_Q$ is limited to those points $\mathbf{x}_I$ which can be connected to $\mathbf{x}_Q$ without intersecting a boundary of the domain.

As can be seen, the cells are independent of the nodes and are arranged in a regular pattern in both dimensions. The cells serve two purposes:

1. they facilitate the identification of nodes which contribute to the discrete L_2 norm at a quadrature point, equation (4),
2. they provide a structure for the numerical quadrature of equations (29).

In each cell, Gauss quadrature is used. The number of quadrature points depends on the number of nodes in a cell. We have used $n_Q \times n_Q$ Gauss quadrature where

$$n_Q = \sqrt{m} + 2 \tag{31}$$

and m is the number of nodes in a cell. The scheme is then shown in Table I.

Note that these two loops assemble the Galerkin equations similar to the finite element method except that the assembly is performed at each quadrature point because each quadrature point can have a different connectivity. The connectivity of a quadrature point depends on the nodes in the domain of influence of the point $\mathbf{x}_Q$. If the nodes are numbered judiciously, for example, by sorting the x-co-ordinates, the $\mathbf{K}$ part of the matrix in equation (28) will be banded.

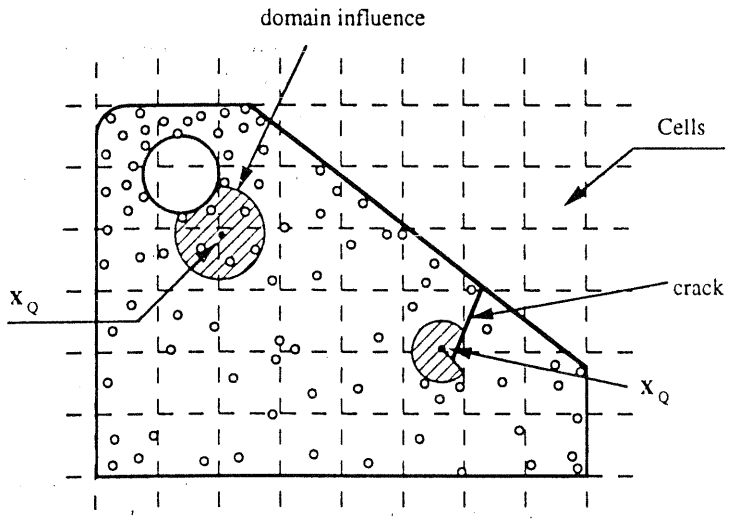

Figure 1. Cell structure for quadrature in EFGM and domains of quadrature point

Table I. Flowchart of EFG

1. loop over cells of domain C
   2. loop over quadrature points $\mathbf{x}_Q$ in cell C
      a. if quadrature point outside physical domain, go to 2g;
      b. check all nodes in cell and surrounding cells to determine the m nodes $\mathbf{x}_I$, $I = 1$ to m in the domain of influence of $\mathbf{x}_Q$;
      c. if a boundary segment exists in the cell around cell C and if $\mathbf{x}_I - \mathbf{x}_Q$ intersects the boundary segment, go to 2g;
      d. compute $\phi_I(\mathbf{x}_Q)$ and $\phi_{I,i}(\mathbf{x}_Q)$ at the quadrature point;
      e. evaluate contributions to equation (29);
      f. assemble contributions to nodes;
      g. end if.
   3. end quadrature point loop
4. end cell loop.

The check in step 2c in Table I is necessary to deal correctly with interior boundaries such as cracks and holes. As shown in the lower right band corner of the example in Figure 1, the domain of influence of a point does not extend across a boundary adjacent to that point. Thus, only those points $\mathbf{x}_I$ which can be connected to $\mathbf{x}_Q$ without intersecting any boundary are in the domain of influence of $\mathbf{x}_Q$.

An important question is the number of cells to be used. We have performed most of our calculations by using $m_c \times m_c$ cells, where

$$m_c = \sqrt{n_N} \tag{32}$$

and n_N is the total number of nodes.

NUMERICAL RESULTS

Several numerical studies of the performance of the EFG method in elasticity and heat conduction were made. The following issues were addressed:

1. the use of the Lagrange multipliers to enforce essential boundary conditions,
2. the effect of assuming $\mathbf{a}(\mathbf{x})$ as a constant in equation (10),
3. the effect of the two choices of weight functions in equations (18) and (19) and its radius of influence,
4. the rates of convergence of the method for various polynomials and node spacings.

Elasticity

Patch test. The first numerical example is the standard patch test, shown in Figure 2. In this patch test, the displacements were prescribed on all outside boundaries by a linear function of x and y on a patch of dimension $L_x = 2$ by $L_y = 2$. Satisfaction of the patch test then requires that the displacement of any interior nodes be given by the same linear function and that the strains and stresses be constant in the patch.

When the essential boundary conditions on the four edges were imposed by Lagrange multipliers, the EFG method exactly passes all patch tests shown in Figure 2(a)-(c) regardless of the choices of weight functions for stable values of the parameter d_{mI}. Note that for the patch test

(b), four cells with the dimension $L_x/2$ by $L_y/2$ were used. Since the node points are randomly distributed, c_I in equation (21) is set to be $\max(L_x/2, L_y/2) = 1$. In the absence of the Lagrange multipliers, i.e. if the essential boundary condition is imposed directly on the trial function at each node on Γ_u via equation (10), the displacements were in error as shown in Table II unless node 9 was in the centre of the patch, and the errors were quite large when the placement of node 9 resulted in a very irregular geometry. The stresses at node 9 were also quite erroneous. Note in that case that the resulting stiffness matrix is not symmetric. Since failure to satisfy the

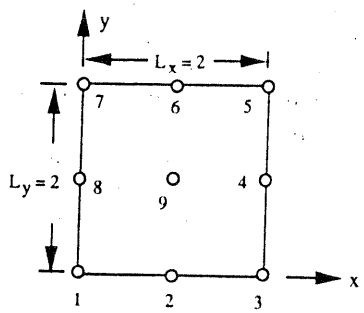

(a) EFG regular data points

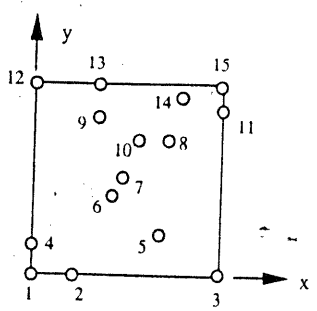

(b) EFG irregular data points

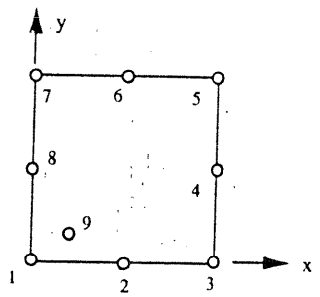

(c) EFG random data point for node 9

Table: Coordinates for patch (b)

nodes	coordinate (x,y)
2	0.3 , 0.
4	0. , 0.2
5	1.2 , 0.4
6	0.8 , 0.9
7	0.9, 1.
8	1.4, 1.2
9	0.5 , 1.3
10	1.1, 1.2
11	2. , 1.8
13	0.8, 2.
14	1.6, 1.9

Figure 2. Nodes used in EFG method for patch tests

Table II. Relative errors at node 9 located randomly for the patch (c) without Lagrange multiplier for essential boundary condition (weight function A with $d_{mI} = 1{\cdot}5$)

Co-ordinates of node 9 (x, y)	Relative error of u_x $[u]$	Relative error of u_y $[v]$	Relative error of σ_x $[sx]$	Relative error of σ_y $[sy]$	Relative error of σ_{xy} $[sxy]$
(1·0, 1·0)	0·	0·	0·	0·	0·
(1·1, 1·1)	3·05%	1·56%	− 0·98%	− 0·77%	− 0·86%
(1·2, 1·0)	4·05%	0·78%	− 1·75%	− 0·53%	− 0·50%
(0·1, 1·8)	35·75%	− 27·97%	85·91%	56·42%	− 70·12%
(1·9, 1·8)	− 35·39%	28·95%	194·59%	142·13%	164·46%
(1·9, 0·1)	− 34·24%	12·13%	134·95%	127·23%	− 130·43%

patch test corresponds to loss of consistency, it is apparent that the imposition of essential boundary conditions by Lagrange multipliers is imperative.

Higher-order patches. The higher-order patches shown in Figure 3 (Reference 11) were used to study the effect of the weight functions, its domain of influence and the effect of accounting for the variation of $\mathbf{a}(\mathbf{x})$ as given in equation (12). In case 1, a uniform axial stress of unit intensity is applied to the right end. The exact solution for this problem with $E = 1$ and $\nu = 0{\cdot}25$ is $u_x = x$ and $u_y = -y/4$. In case 2, a linearly varying normal stress is applied to the right end and skew symmetric boundary conditions are imposed along the bottom edge. The exact solution for this problem with $E = 1$ and $\nu = 0{\cdot}25$ is $u_x = xy$ and $u_y = (4x^2 - y^2)/8$. The relative errors of displacements u_x and u_y at point A are considered for case 1 and case 2, respectively, which are given in Figures 4–7. The linear basis function in equation (3a) is used in Figures 3–5 and the quadratic basis function in equation (3b) is used in Figure 7. As can be seen from Figures 4 and 7, the accuracy of the solution with the conical weight function (WFB) is generally poorer than with the exponential weight function (WFA). Furthermore, the accuracy of the method is impaired substantially if the polynomial coefficients $\mathbf{a}(\mathbf{x})$ are assumed to be constants, i.e. when the derivatives $\mathbf{a}_{,i}$ are not included in the Galerkin equations.

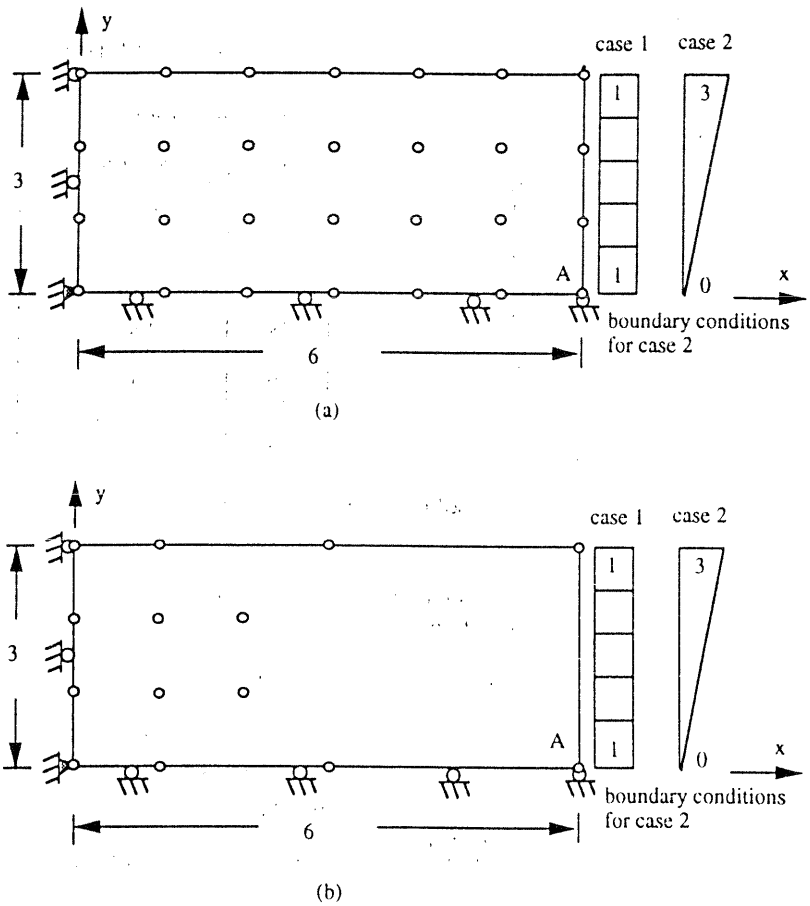

Figure 3. Data points (nodes) in EFG method for Taylor *et al.*[11] higher-order patches

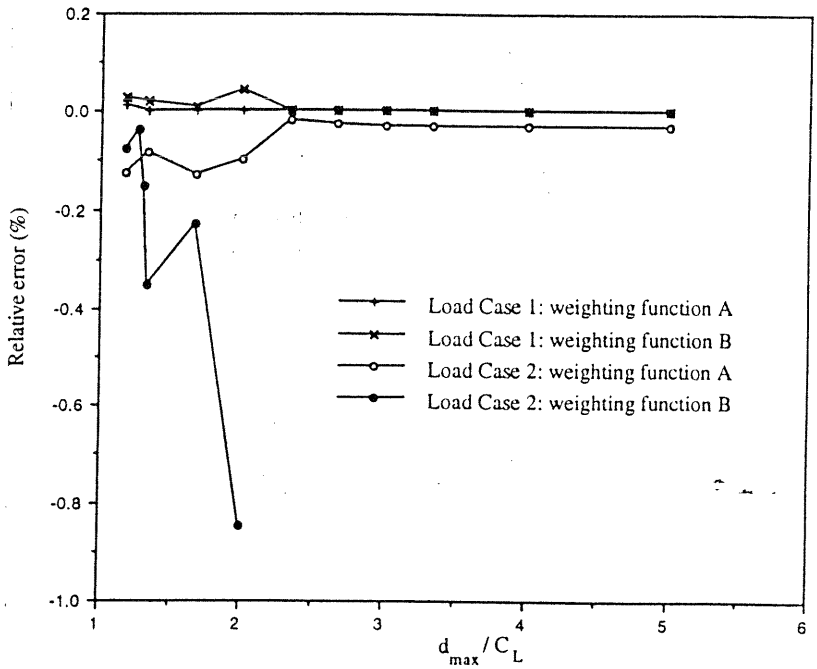

Figure 4. Relative errors at point A for load cases 1 and 2 with non-uniform nodes (Figure 3(b))

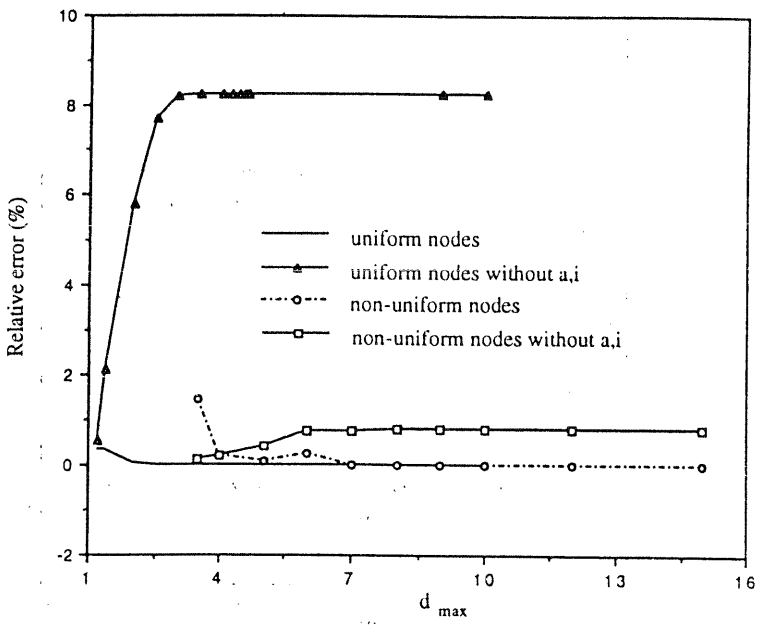

Figure 5. Relative errors at point A for load case 1 with uniform nodes (Figure 3(a)), non-uniform nodes (Figure 3(b)) and weight function A

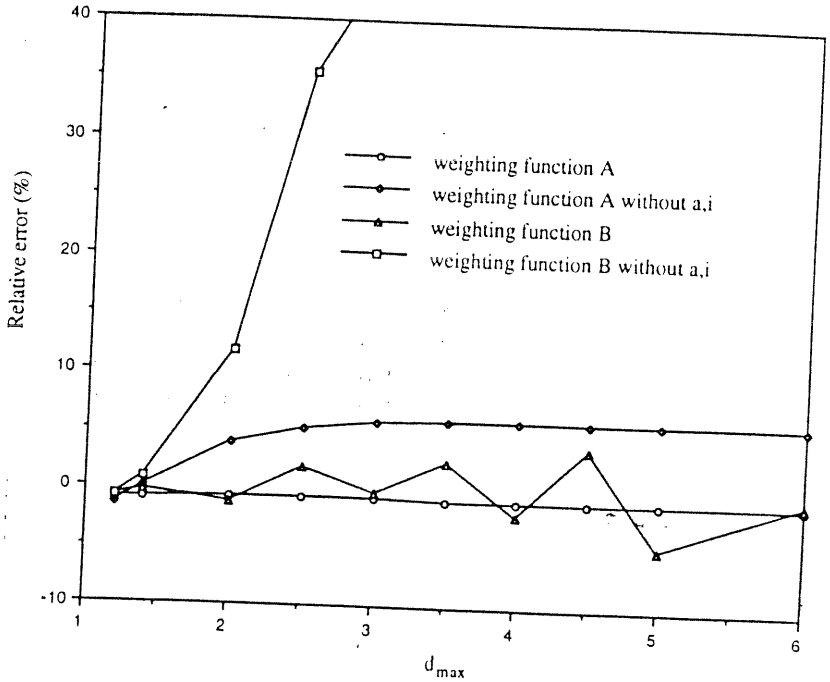

Figure 6. Relative errors at point A for load case 2 with uniform nodes (Figure 3(a))

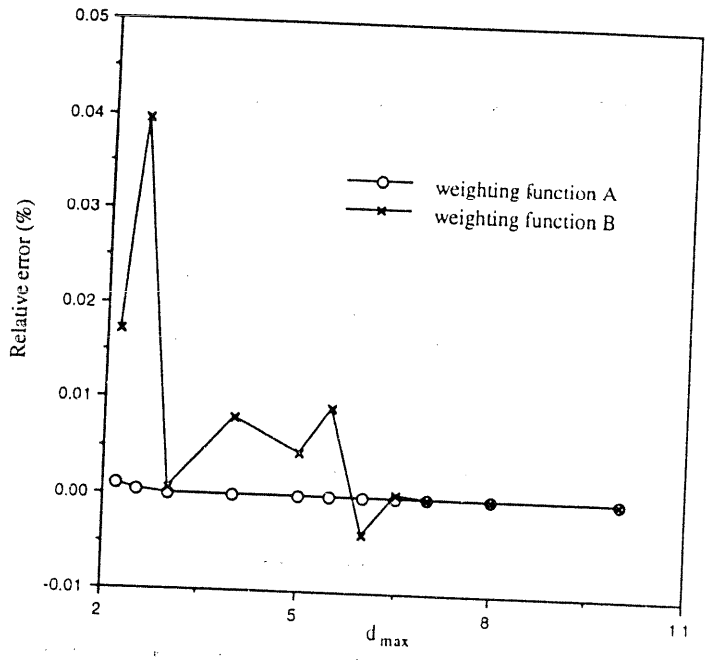

Figure 7. Relative errors at point A with quadratic basis function for load case 2 with uniform nodes (Figure 3(a))

Beam. The behaviour of the EFG method was also studied in the cantilever beam problem, for which the following exact solution is given by Timoshenko and Goodier:[12]

$$u_x = -\frac{P}{6\bar{E}I}\left(y - \frac{D}{2}\right)[(6L - 3x)x + (2 + \bar{\nu})(y^2 - 2Dy)] \tag{33a}$$

$$u_y = \frac{P}{6\bar{E}I}[3\bar{\nu}(y^2 - 2Dy + \tfrac{1}{2}D^2)(L - x) + \tfrac{1}{4}(4 + 5\bar{\nu})D^2x + (L - \tfrac{1}{3}x)3x^2] \tag{33b}$$

where

$$I = \frac{D^3}{12} \tag{33c}$$

$$\bar{E} = \begin{cases} E & \text{for plane stress} \\ E/(1 - \bar{\nu}^2) & \text{for plane strain} \end{cases} \tag{33d}$$

$$\bar{\nu} = \begin{cases} \nu & \text{for plane stress} \\ \nu/(1 - \nu) & \text{for plane strain} \end{cases} \tag{33e}$$

The stresses corresponding to (33) are

$$\sigma_x(x, y) = -\frac{P}{I}(L - x)(y - \tfrac{1}{2}D) \tag{34a}$$

$$\sigma_y(x, y) = 0 \tag{34b}$$

$$\sigma_{xy}(x, y) = -\frac{Py}{2I}(y - D) \tag{34c}$$

The problem was solved for the plane strain case with $E = 3{\cdot}0 \times 10^7$, $D = 1$ and $L = 8$. Both a regular mesh of nodes and an irregular mesh of nodes shown in Figure 8 were considered. The space integration was performed by using four zones in the vertical direction and ten zones in the horizontal direction. In each zone, 4×4 Gauss quadrature was used to evaluate the stiffness of the EFG. EFG solutions were obtained with linear, quadratic and cubic basis functions using the same mesh points and the same exponential weight function.

The deflection at point A, w^{NUM}, is compared to the analytical result w^{EXACT} in Table III with $\alpha = 2$ and $d_{mI} = 6c$ in the exponential weight function, equation (18). For comparison, finite

Table III. Tip deflection ratio for the beam problem

$w^{\text{NUM}}/w^{\text{EXACT}}$ at point A				
	Regular mesh (data points)		Irregular mesh (data points)	
Method	Case 1 plane strain $\nu = 0{\cdot}25$	Case 2 plane strain $\nu = 0{\cdot}4999$	Case 1 plane strain $\nu = 0{\cdot}25$	Case 2 plane strain $\nu = 0{\cdot}4999$
FEM: Q4	0·824	0·027	0·607	0·029
FEM: QBI	0·996	0·988	0·745	0·683
EFG: linear	0·999	1·045	0·997	0·982
EFG: quadratic	1·00	1·002	0·999	0·997
EFG: cubic	1·00	1·00	1·00	1·00

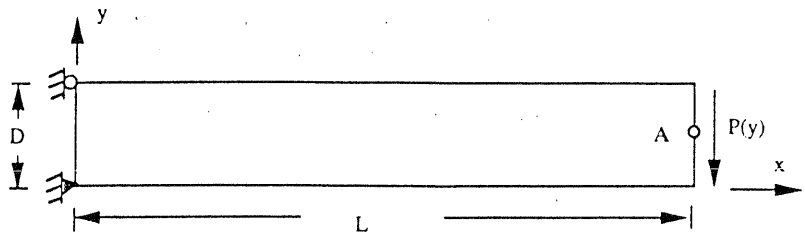

a). Cantilever beam

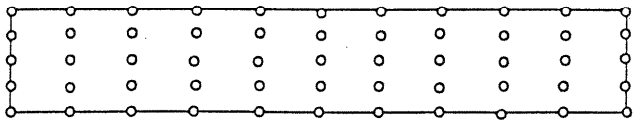

b). regular data points

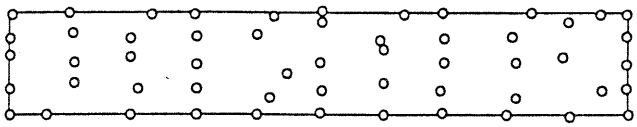

c). irregular data points for EFGM and mesh for FEM

Figure 8. Cantilever beam with a parabolic-shear end load and data points

element solutions were also obtained using the standard 4-node quadrilateral with full 2×2 Gauss quadrature, Q4, and a mixed element QBI.[13] In the latter, the higher-order terms in the strain field were constructed so that locking is avoided for nearly incompressible materials and convergence is enhanced for beam bending.

A noteworthy feature of the EFG results is that they do not exhibit any locking, even though nothing was done to modify its behaviour in the nearly incompressible case, $\nu = 0{\cdot}4999$ in plane strain. Note that the Q4 element locks in this situation. The EFG method, if anything, is somewhat flexible.

Figure 9 shows the shear stress σ_{xy} for $\nu = 0{\cdot}25$ at $x = L/2$ obtained by EFG method. The solution obtained by QBI is also included. Note that the stresses obtained by the finite element solution is not continuous along the line $x = L/2$. The discontinuous stress σ_{xy} is denoted as $\sigma_{xy}(+)$ in the right element and $\sigma_{xy}(-)$ in the left element in Figure 9. It can be seen that the stress field obtained by EFG is much better than that obtained by FEM. It is noted from Figure 10 that the EFG solution satisfies the traction-free boundary conditions (i.e. at $y = 0$ and $y = 1$) very well.

For the convergence studies, we define the displacement norm and energy norm as follows:

$$\text{displacement norm} = \left\{ \int_\Omega (\mathbf{u}^{\text{NUM}} - \mathbf{u}^{\text{EXACT}})^{\text{T}} (\mathbf{u}^{\text{NUM}} - \mathbf{u}^{\text{EXACT}}) \, \mathrm{d}\Omega \right\}^{1/2} \tag{35a}$$

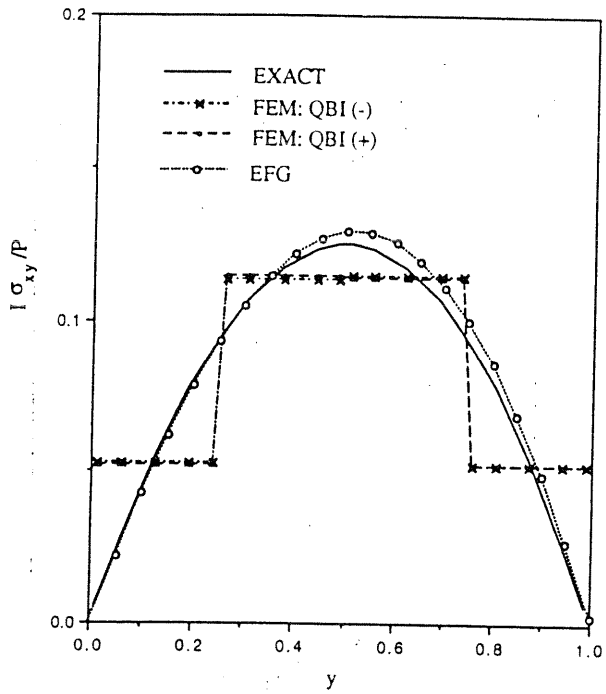

Figure 9. Distribution of shear stress σ_{xy} at $x = L/2$ for $\nu = 0{\cdot}25$ in beam problem with irregular points

$$\text{energy norm} = \left\{\frac{1}{2}\int_{\Omega} (\varepsilon^{\text{NUM}} - \varepsilon^{\text{EXACT}})^{\text{T}}\, \mathbf{D}(\varepsilon^{\text{NUM}} - \varepsilon^{\text{EXACT}})\, d\Omega\right\}^{1/2} \tag{35b}$$

The convergence with mesh refinement is shown in Figures 10 and 11 ($c = c_I$, $\alpha = 1$) and Figures 12 and 13 ($c = 2c_I$, $\alpha = 2$). The convergence rates are indicated by R in the figures, and $h = c_I$ which is equivalent to the maximum element size in the finite element method in this case. It is observed that the convergence rates of the EFG method for both linear and quadratic basis function exceeds the corresponding convergence rates for finite elements, which are 2 and 3, respectively, for linear and quadratic elements. It is noted that the convergence rates depend on the value of c. However, for a given value of c, the convergence rates still exceed those of finite elements. Figures 14 and 15 show the convergence rates for the plane strain case $\nu = 0{\cdot}25$ with $c = 1$. It is startling that the convergence rates of EFG exceed those of finite elements significantly. Since we were not able to obtain the optimal value of c by theory, the definition of $c = c_I$ in equation (21) is only an empirical recommendation.

Hole in an infinite plate. This problem is a portion of an infinite plate with a central circular hole subjected to a unidirectional tensile load of 1·0 in the x direction as shown in Figure 16. Due to symmetry, only the upper right quadrant of the plate is modelled. Plane strain conditions were assumed with $E = 1{\cdot}0 \times 10^3$ and $\nu = 0{\cdot}3$. Symmetry conditions were imposed on the left and bottom edges, and the inner boundary at $a = 1$ is traction-free. The exact solution for the stresses is

$$\sigma_x(x, y) = 1 - \frac{a^2}{r^2}\{\tfrac{3}{2}\cos 2\theta + \cos 4\theta\} + \frac{3a^4}{2r^4}\cos 4\theta \tag{36a}$$

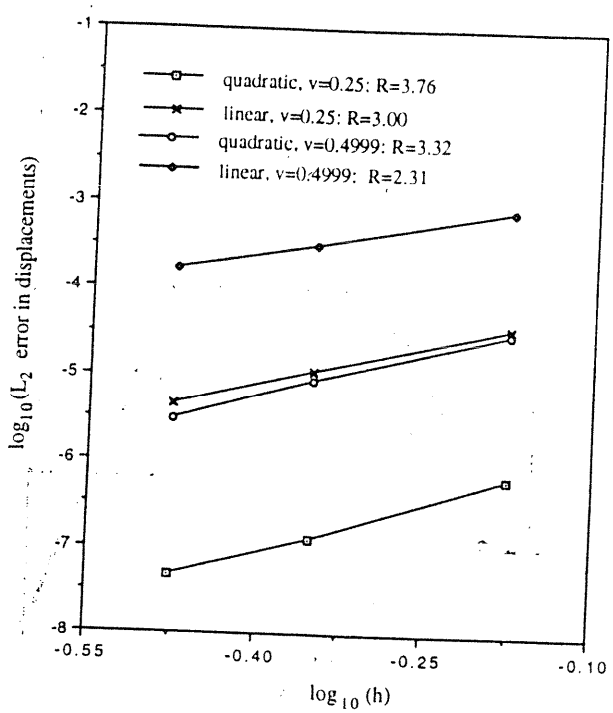

Figure 10. Convergence rates in L_2 norm of error in displacements for the plane strain cases $\nu = 0{\cdot}25$ and $\nu = 0{\cdot}4999$ with $\alpha = 1$

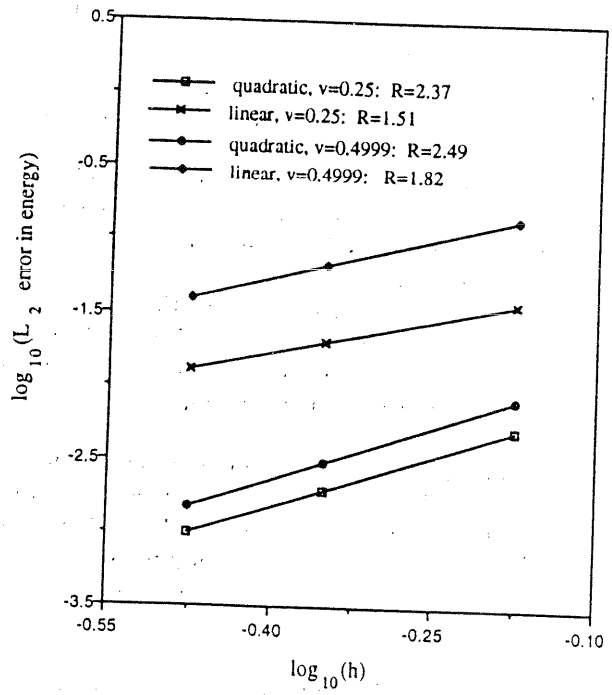

Figure 11. Convergence rates in energy-norm for the plane strain cases $\nu = 0{\cdot}25$ and $\nu = 0{\cdot}4999$ with $\alpha = 1$

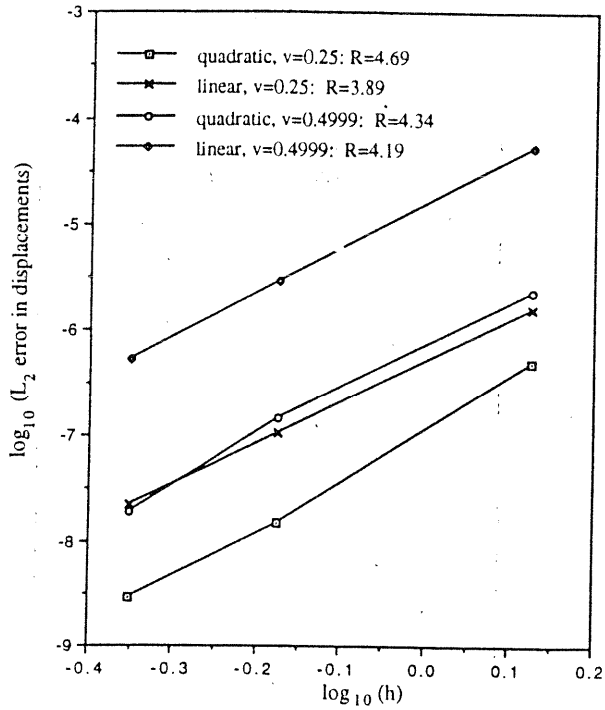

Figure 12. Convergence rates in L_2 norm of error in displacements for the plane strain cases $\nu = 0{\cdot}25$ and $\nu = 0{\cdot}4999$ with $\alpha = 2$

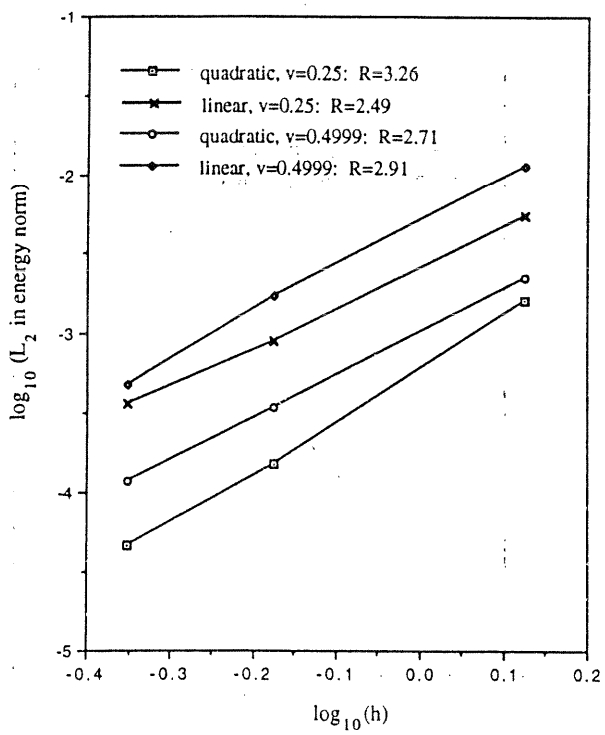

Figure 13. Convergence rates in energy-norm for the plane strain cases $\nu = 0{\cdot}25$ and $\nu = 0{\cdot}4999$ with $\alpha = 2$

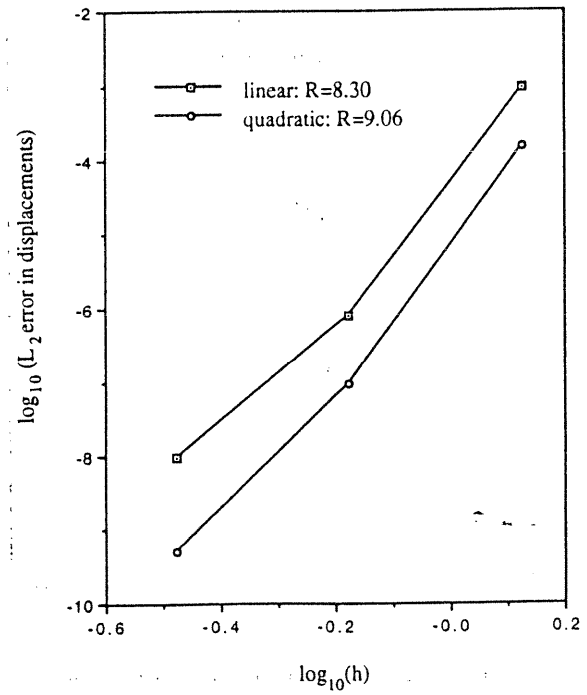

Figure 14. Convergence rates in L_2 norm of error in displacements for the plane strain case $\nu = 0{\cdot}25$ with $c = 1$ in equation (20)

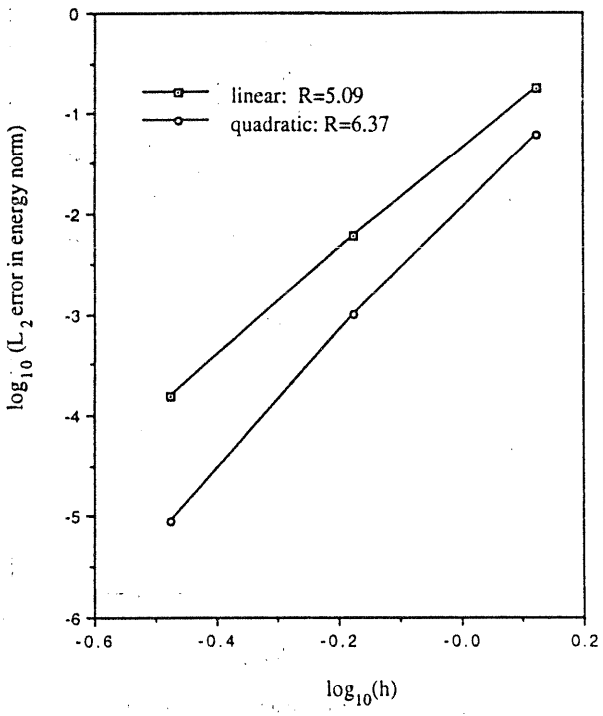

Figure 15. Convergence rates in energy-norm for the plane strain case $\nu = 0{\cdot}25$ with $c = 1$ in equation (20)

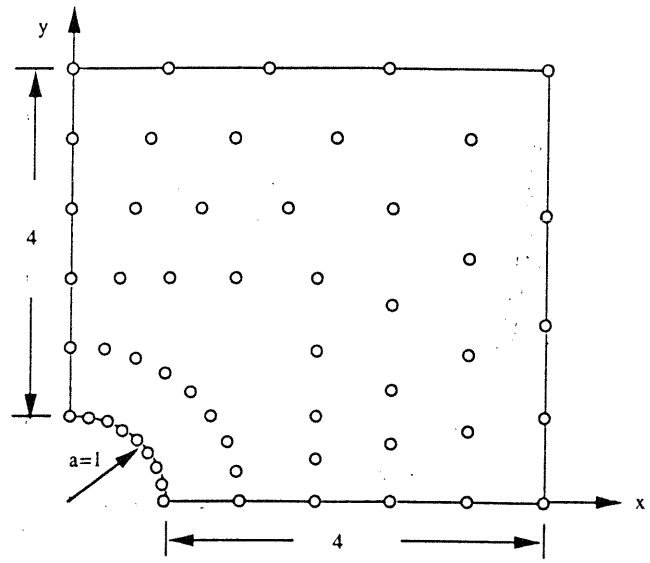

(a). initial data points for EFGM

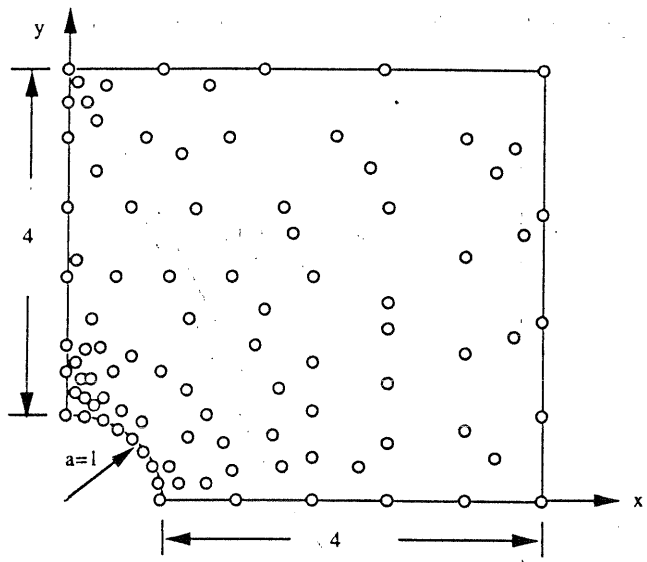

(b). data points for EFGM

Figure 16. A square plate as a portion of an infinite plate with a central circular hole subjected a unidirectional tensile load of 1·0 in the x direction

$$\sigma_y(x,y) = -\frac{a^2}{r^2}\{\tfrac{1}{2}\cos 2\theta - \cos 4\theta\} - \frac{3a^4}{2r^4}\cos 4\theta \tag{36b}$$

$$\sigma_{xy}(x,y) = -\frac{a^2}{r^2}\{\tfrac{1}{2}\sin 2\theta + \sin 4\theta\} + \frac{3a^4}{2r^4}\sin 4\theta \tag{36c}$$

where (r,θ) are the usual polar co-ordinates and θ is measured from the positive x axis

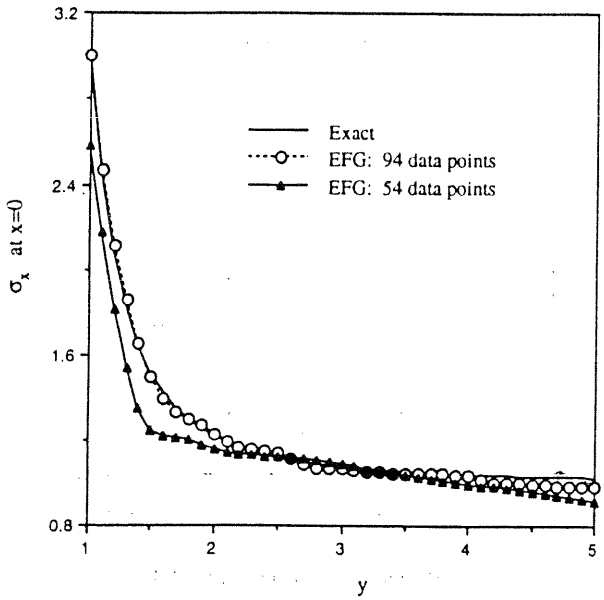

Figure 17. Comparison between the exact solution and EFGM results for stress σ_x at $x = 0$

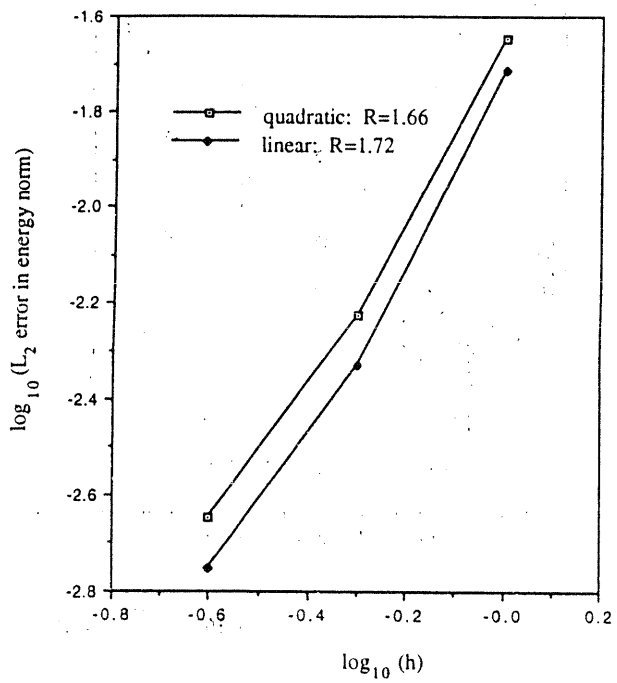

Figure 18. Convergence rates in energy-norm for plane strain case ($\nu = 0{\cdot}3$)

counterclockwise. Traction boundary conditions given by the exact solution (36) were imposed on the right ($x = 5$) and top ($y = 5$) edges.

The initial mesh of 54 nodes is shown in Figure 16(a). Subsequently, the number of nodes was increased to 94 as shown in Figure 16(b). The weight function in equation (18) with $c = c_I$ and $d_{mI} = 4c$ is used. The stress σ_x at $x = 0$ obtained by EFG method is given in Figure 17. The result using only the nodes in Figure 16(a) is also shown in Figure 17 for comparison. As in the convergence studies, only the energy norm is calculated and the results are shown in Figure 18. For this problem, the quadratic basis function surprisingly is not as good as the linear basis function.

Fracture Example. This problem is a rectangular plate with an edge-crack as shown in Figure 19. In the EFG model, twofold symmetry is used to reduce the problem as shown in Figure 20. Several node arrangements were used around the crack tip as shown. The mode I stress intensity factor, K_I, was evaluated by using the J-integral over the contour shown. A 10×10 array of cells were used and 3×3 Gauss quadrature was used in all cells except those around the crack tip, where it was 6×6.

The normalized results for K_I for the various meshes around the crack tip are shown. As can be seen, the nodal arrangement around the crack tip can be quite independent of the nodal arrangement outside the crack tip area. By using 39 nodes in the crack tip area, error is reduced to less than 1 per cent. The benchmark was $K_I = 2{\cdot}358$ given in Tada *et al.*[14] Linear basis functions with an exponential weight functions were used. These results suggest a simple procedure for

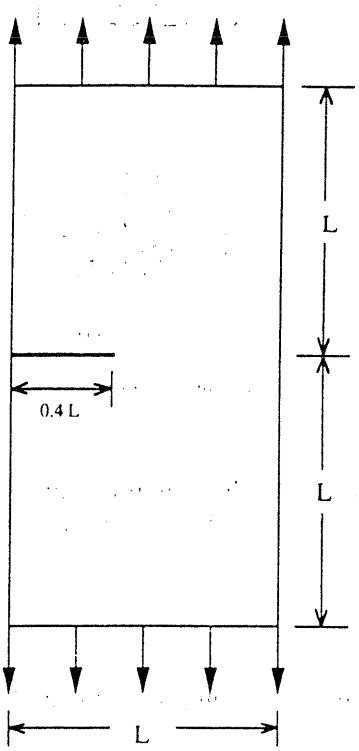

Figure 19. Plate with edge crack under uniaxial stress

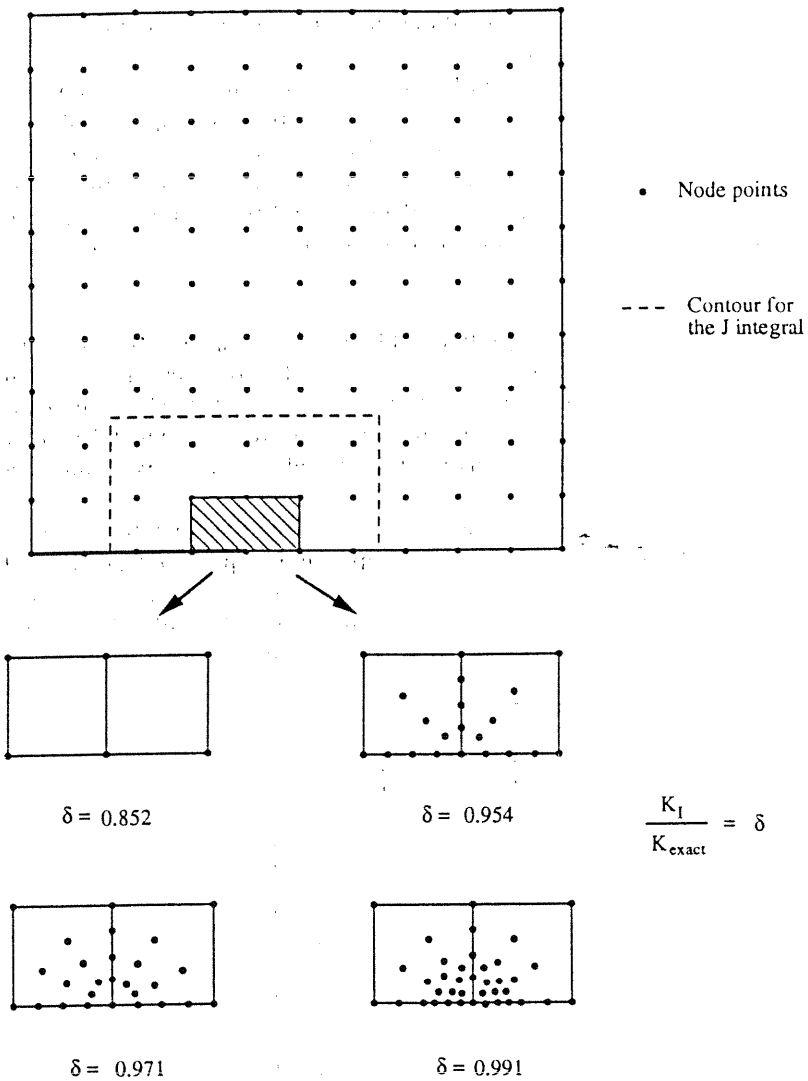

Figure 20. Node point arrangements and results for edge crack problem

checking stress intensity factors in EFG method: simply adding nodes in the vicinity of the crack tip, and if K_I changes significantly, add more. Because no element connectivities are needed, this procedure is quite simple.

Steady-state heat conduction

High-gradient problem. The heat conduction problem considered here is a rectangular plate ($0{\cdot}5 \times 6$ in^2) with heat source

$$b(x, y) = 2s^2 \operatorname{sech}^2 [s(y - 3)] \tanh [s(y - 3)] \tag{37}$$

The boundary conditions are given by

$$T = -\tanh(3s) \quad \text{at } y = 0 \tag{38a}$$

$$T = \tanh(3s) \quad \text{at } y = 6 \tag{38b}$$

$$T_{,x} = 0 \quad \text{at } x = -0{\cdot}25 \text{ and } x = 0{\cdot}25 \tag{38c}$$

The exact solution for this problem is

$$T = \tanh[s(y - 3)] \tag{39}$$

As shown in Belytschko and Lu,[15] this problem has a high gradient near $y = 3$. In the above, s is a free parameter; as s increases, the field $T_{,y}$ has an increasing gradient.

In the area ($2{\cdot}5 \leqslant y \leqslant 3{\cdot}5$) where the high gradient occurs, a regular array of 50×5 nodes and quadratic basis functions were used in the moving least-squares interpolant. In the rest of the domain, 20×5 nodes and linear basis functions were used. The weight function used here is given by equation (18), where c is defined by equation (21) with $\alpha = 1$. Figure 21 is the EFG results of temperature along $x = 0$, which show a good agreement with the exact solution.

The problem was also solved by 4-node finite elements with a uniform mesh (240×10). For comparison, we use linear basis function given in equation (3a) and used the same nodes for the finite element mesh as in the EFG. The weight function in equation (18) is used with c defined by equation (21) and $\alpha = 1$. Figure 22 shows that the results for the gradient $T_{,y}$ by EFG are much better than those by FEM, especially for the large s.

The rates of convergence in the temperature norm and the gradient norm were studied:

$$(\text{temperature norm})^2 = \int_\Omega (T^{\text{exact}} - T^{\text{num}})^2 \, d\Omega \tag{40}$$

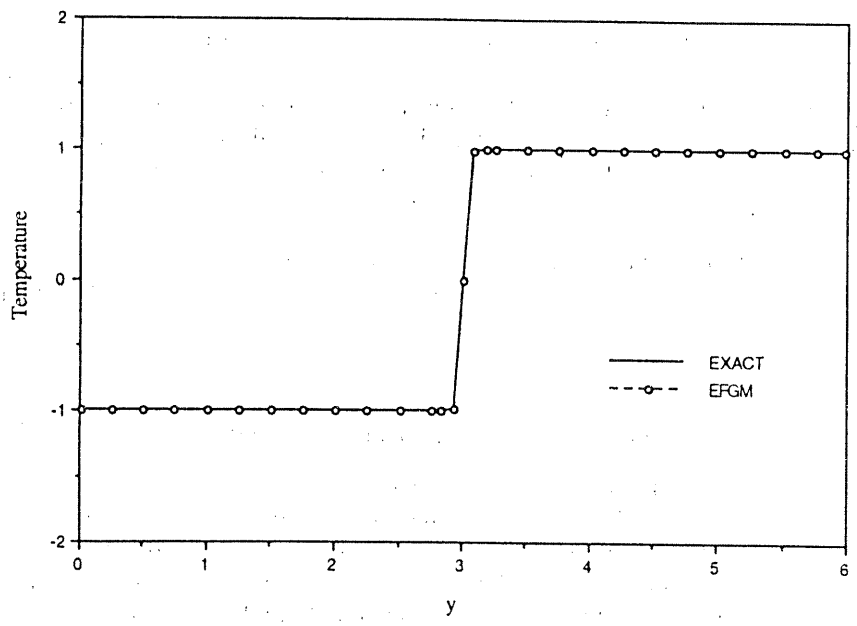

Figure 21. Comparison between exact solution and EFGM results for the high-gradient problem with $s = 40$

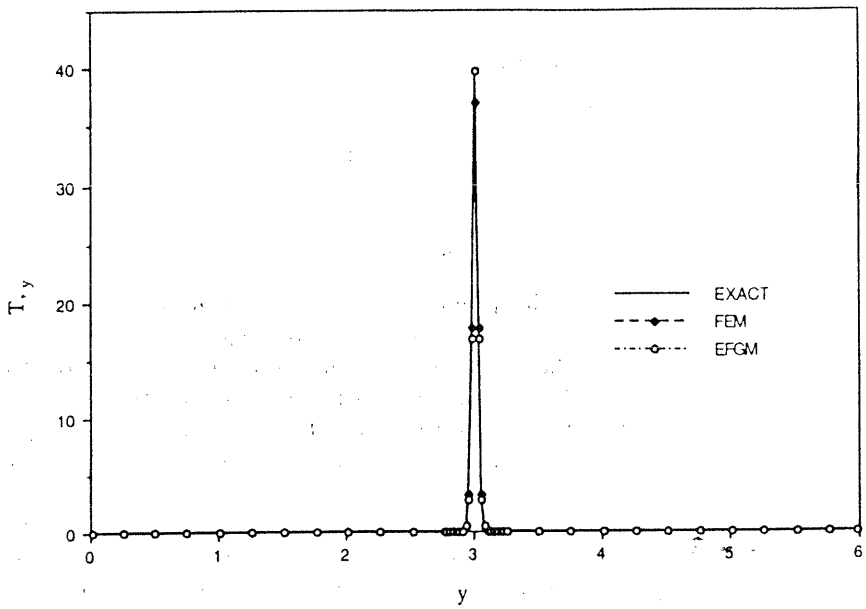

Figure 22. Comparison among exact solution, EFGM and FEM results of gradient field for the high-gradient problem with $s = 40$

$$(\text{gradient norm})^2 = \int_\Omega \{(T_{,x}^{\text{exact}} - T_{,x}^{\text{num}})^2 + (T_{,y}^{\text{exact}} - T_{,y}^{\text{num}})^2\}\, d\Omega \tag{41}$$

The uniform meshes are 30×2, 60×4, 120×8 and 240×16 and the results are shown in Figures 23–26. The convergence rates in the EFG always exceed the FEM, which are 2 for the temperature norm and 1 for the gradient norm, respectively. In the EFG method, different choices of the weight function result in the different convergence rates. In the case of weight function A (equation (18)) with d_m equal to $3c$ and c defined by equation (21) with $\alpha = 1$, the convergence rates are around 3 for the temperature norm and 2 for the gradient norm, respectively, although these depend on s. For weight function B defined by equation (19) with d_m equal to 1·15 times element length, the convergence rates are 2·3 for the temperature norm, and 1·2 for the gradient norm, respectively.

Thus, the EFG always exhibits higher convergence rates than those of the FEM, although it depends on the choice of weight functions. Several other weight functions, such as B-splines and triangular functions, were also tested. In all the cases, the convergence rates for the temperature norm and the gradient norm exceeded 2 and 1, respectively.

DISCUSSION AND CONCLUSIONS

Some aspects of the element-free Galerkin method (EFGM) have been studied. This method was introduced for solution of partial differential equations by Nayroles *et al.*[1] Their implementation of the method was motivated primarily by simplicity, and used rather rough quadrature.

In this implementation, more accurate but nevertheless versatile quadrature methods are used. As a consequence, surprising accuracy can be achieved. In fact, one of the most startling discoveries in these studies is the high rates of convergence which were observed, and that nearly

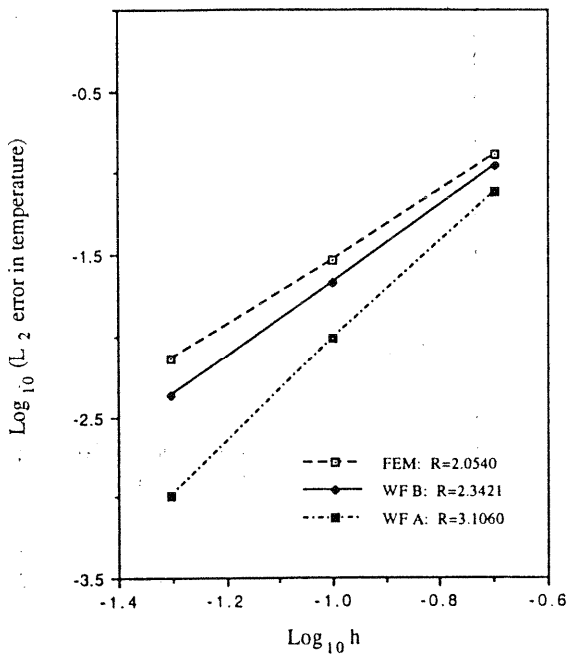

Figure 23. Convergence rates of the temperature norm for the high-gradient problems with $s = 10$

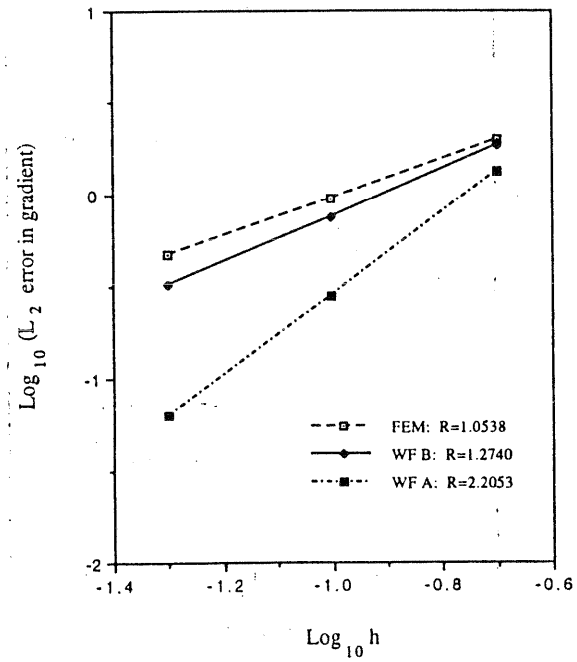

Figure 24. Convergence rates of the gradient norm for the high-gradient problems with $s = 10$

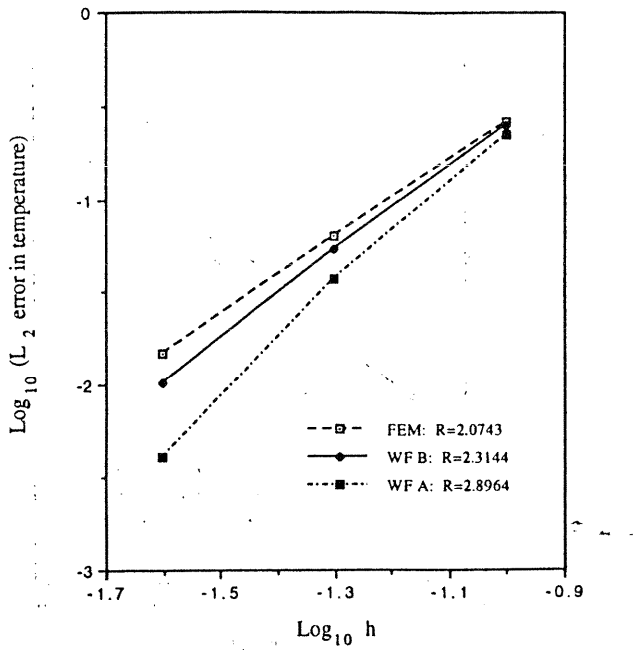

Figure 25. Convergence rates of the temperature norm for the high-gradient problems with $s = 40$

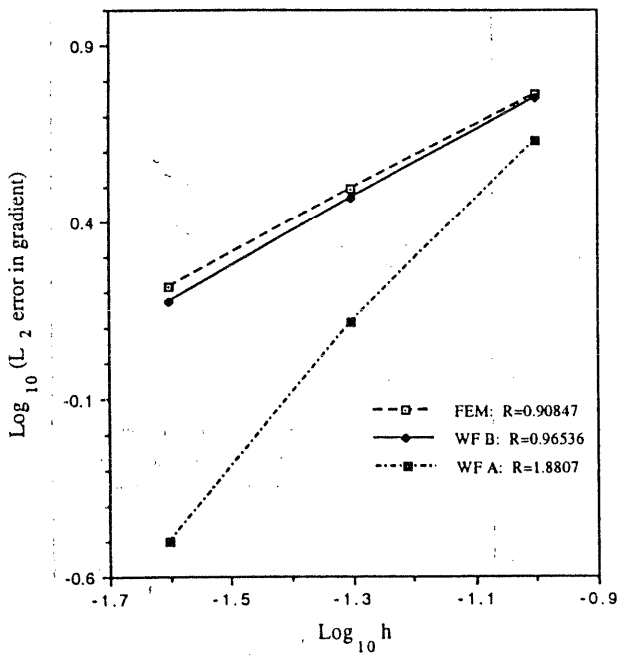

Figure 26. Convergence rates of the gradient norm for the high-gradient problems with $s = 40$

incompressible materials can be treated by the method without any modification and without any evidence of locking.

Furthermore, the method appears to be very effective for crack problems. Results with 1 per cent accuracy were obtained for an example fracture problem. The method is particularly attractive for this class of problems because progressively growing cracks can be easily modelled. It is only necessary to move the fine mesh of nodes through the rest of the mesh, which is quite easy since element connectivities do not need to be developed and performance seems to be quite independent of nodal point arrangement, i.e. whereas in finite element methods, skewed elements degrade performance, EFG performance seems to be minimally affected by irregular placement of nodes.

The achievement of high accuracy requires three features not used by Nayroles *et al.*[1]

1. the use of Lagrange multipliers to enforce the essential boundary condition,
2. accurate evaluation of the derivatives,
3. higher-order quadrature in space.

It was found that the performance of the method depends on the weight function: the exponential function, which is essentially a truncated Gauss distribution, performs far better than a conical weight function. In the latter, the results are more sensitive to the value of d_m, which severely limits its usefulness.

Another advantage of the method is that it requires no postprocessing for the output of strains and stresses or other field variables which are derivatives of the primary-dependent variables since these quantities are already very smooth. Thus, whereas in finite element methods, various types of postprocessing, such as L_2 projection, are necessary in order to obtain a smooth stress field suitable for contour plotting or colour plotting, in the element-free Galerkin method this is totally unnecessary.

The method offers tremendous potential in industrial applications because it is not necessary to mesh nodes and elements. The numerical discretization is defined simply inserting a completely unstructured mesh of nodes in the object. This facilitates the enhancement of resolution in the regions of the solid where it is needed because transition elements need not be set up. It also offers substantial promise in the implementation of adaptivity.

The advantages of the method do not come without some costs. The construction of an underlying zone structure for purposes of numerical quadrature can be awkward if there are large differences in node spacing within one mesh. The use of Lagrange multipliers complicates the solution process, since special solvers with variable bandwidth and which do not take advantage of positive definiteness need to be employed. This can be later remedied to some extent by the use of perturbed Lagrangian or penalty methods. Nevertheless, the potential benefits in many problems are so attractive that this method deserves consideration.

ACKNOWLEDGEMENT

The support of National Science Foundation and the Office of Naval Research to Northwestern University is gratefully acknowledged.

Note added in proof:

In the hole example, Figure 16, a radial cell structure was used with the boundaries of the extended domain given by $1 \leqslant r \leqslant (25 + y^2)^{1/2}$ for $0 \leqslant \theta \leqslant \pi/4$, $1 \leqslant r \leqslant (25 + x^2)^{1/2}$ for $\pi/4 \leqslant \theta \leqslant \pi/2$. A 5×8 cell structure was used in the r-θ domain.

The average number of nodes in the domain of influence in the hole problem which result with $d_{mI} = 4c$ (as given in the paper) is 48. This gives the MLS interpolant a higher order even with a linear basis, which accounts for the high rate of convergence.

REFERENCES

1. B. Nayroles, G. Touzot and P. Villon, 'Generalizing the finite element method: diffuse approximation and diffuse elements', *Comput. Mech.*, **10**, 307–318 (1992).
2. P. Lancaster and K. Salkauskas, 'Surfaces generated by moving least squares methods', *Math. Comput.*, **37**, 141–158 (1981).
3. D. H. McLain, 'Drawing contours from arbitrary data points', *Comput. J.*, **17**, 318–324 (1974).
4. W. J. Gordon and J. A. Wixom, 'Shepard's method of 'metric interpolation' to bivariate and multivariate data', *Math. Comput.*, **32**, 253–264 (1978).
5. R. E. Barnhill, 'Representation and approximation of surfaces', in *Mathematical Software III*, Academic Press, New York, (1977), pp. 69–120.
6. R. A. Nay and S. Utku, 'An alternative for the finite element method', *Proc. Int. Conf. held at the University of Southampton*, Vol. I, 1972.
7. R. A. Gingold and J. J. Monaghan, 'Smoothed particle hydrodynamics: theory and application to non-spherical stars', *Mon. Not. Roy. Astron. Soc.*, **181**, 375–389 (1977).
8. O. C. Zienkiewicz and R. L. Taylor, *The Finite Element Method*, 4th Edn, McGraw-Hill, London, 1991.
9. D. J. Benson and J. O. Hallquist, 'A simple surface contact algorithm for the postbuckling analysis of shell structures', *Report to the University of California at San Diego*, CA, 1987.
10. T. Belytschko and J. I. Lin, 'A three-dimensional impact-penetration algorithm with erosion', *Comput. Struct.*, **25**, 95–104 (1987).
11. R. L. Taylor, P. J. Beresford and E. L. Wilson, 'A non-conforming element for stress analysis', *Int. j. numer. methods eng.*, **10**, 1211–1219 (1976).
12. S. P. Timoskenko and J. N. Goodier, *Theory of Elasticity*, 3rd Edn, McGraw-Hill, New York, 1970.
13. T. Belytschko and W. E. Bachrach, 'Efficient implementation of quadrilaterals with high coarse-mesh accuracy', *Comput. Methods Appl. Mech. Eng.*, **54**, 279–301 (1986).
14. H. Tada, P. C. Paris and G. R. Irwin, *The Stress Analysis of Cracks Handbook*, Del Research Corporation, Hellertown, PA, 1973.
15. T. Belytschko and Y. Y. Lu, 'A curvilinear spectral overlay method for high gradient problems', *Comput. Methods Appl. Mech. Eng.*, **95**, 383–396.